DAMPING MEASUREMENT AND SOLAR RADIATION PRESSURE VALIDATION OF FLEXIBLE, HIGH AREA-TO-MASS RATIO DEBRIS MODEL

Mr Sittiporn Channumsin
School of Engineering, University of Glasgow, United Kingdom
s.channumsin.1@research.gla.ac.uk

Dr Matteo Ceriotti
School of Engineering, University of Glasgow, United Kingdom
matteo.ceriotti@glasgow.ac.uk

Dr Gianmarco Radice
School of Engineering, University of Glasgow, United Kingdom
Gianmarco.Radice@glasgow.ac.uk

Dr Ian Watson
School of Engineering, University of Glasgow, United Kingdom
Ian.Watson@glasgow.ac.uk

Multilayer insulation (MLI) is thought to be a new type of space debris located in near geosynchronous orbit (GEO). Observation data indicates that these objects exhibit reflection properties and high area-to-mass (HAMR) ratio. Moreover, their area-to-mass (AMR) ratio changes over time, suggesting a high level of flexibility due to extremely low structural strength. As a result, the long term orbital dynamics and rapid attitude motion are substantially affected by GEO environmental perturbations. Previous work by the authors effectively modelled the flexible debris using multibody dynamics. This paper presents a methodology to determine the dynamic properties of thin membranes with the aim to validate the deformation of the flexible model. Experiments are performed in a high-vacuum chamber (10^{-4} mbar) to significantly decrease air friction inside, which a thin membrane is hinged at one end but free at the others. A free motion test is used to determine the damping characteristics and natural frequency of the thin membrane via logarithmic decrement and frequency response. The membrane is allowed to swing freely in the chamber and the motion is tracked by a static camera. The motion is tracked through an optical camera, and a Kalman filter technique is implemented in the tracking algorithm to reduce noise and increase the tracking accuracy of the oscillating motion. Then, the effect of the solar radiation pressure of the thin membrane is investigated: a high power spotlight (500-2000 W) is used to illuminate the sample and any displacement of the thin membrane is measured by means of a high-resolution laser sensor. Analytic methods from the natural frequency response and Finite Element Analysis (FEA) including multibody simulations of both experimental setups are used for the validation of the flexible model by comparing with the experimental results of amplitude decay, natural frequencies and deformation. The experimental results show good agreement with finite element methods.

I. INTRODUCTION

A new population of space debris type in Geostationary synchronous orbit (GEO), which have high area-to-mass ratio (HAMR) and are extremely sensitive to perturbations (especially of non-conservative perturbations) was detected in 2004 by Schildknecht [1-3]. The multi-layer insulation (MLI) is one possible source of these debris objects, coming from explosion, collision and delamination of spacecraft [4-6]. The orbital evolution of HAMR objects, using a cannonball model, where the area-to-mass (AMR) ratio is constant and the attitude motion ignored, has been studied in GEO under perturbations in the long term period. [7-10]. The cannonball model may not be suitable for HAMR objects. Real measurements indicate that the AMR change in time [11]. Further investigation by Früh [12, 13] studied their orbits by the coupling attitude and orbit motions. This investigation determined as a rigid flat plate and a curl plate indicates that the different attitude motion disturbed by torque, which is induced by the Earth's shadow, self-shading and non-uniform reflection properties, results in significant changes in the inclination and eccentricity.

Nevertheless, all studies assume the HAMR objects are rigid bodies. Their constant AMR leads to less accurate propagation of the evolution of the orbital dynamics for this debris type. A more accurate shape, therefore, will provide more precise the prediction. Jay [14] studied the solar radiation effects on the shape changing. That HAMR model is capable to change in five configurations. The condition of the change depends on spin rates. The debris will behave like a perfectly flat rigid object when a shape is changed in the final figure (flat plate). This investigation highlights that the cannonball is not suitable to approximate the orbital dynamics of this debris and supports the fact that the SRP torque highly affects the fast attitude dynamics of this debris type. However, this model does not behave a deformed object for all time of propagation.

In a previous work by the authors [15], a model for the flexible membranes was proposed, consisting of a series lump masses, connected through rigid rods. The masses include rotational springs and dampers to model the flexibility of the thin membrane. The results of this investigation showed the irregular and fast rotation including the continuously changing shape at each time step of the propagation. Solar radiation pressure significantly disturbs the orbital dynamics, generates unstable attitude motion and leads to deform the model.

In order to determine the bending stiffness and damping of the membrane, this paper presents a flexible model by using multibody dynamics and uses a free vibration logarithm decay method (free motion experiment) to determine the damping characteristics of the real membrane [16, 17] and Fast Fourier transform (FFT) to calculate their natural frequency. Then, a further experiment (forced motion experiment) is performed to validate the multibody model by comparing the effect of solar radiation pressure with the finite element analysis (FEA) model.

II. MULTIBODY MODEL

The deformed model of this study is modelled as three lump masses connected with rigid rods ($L_{rod} = L_1 = L_2 = 0.10$). The 2nd lump mass consists of rotational spring and damper. Based on both free motion and forced motion experiments, the multibody model in Fig 1 is fixed with one side on the top of the vacuum chamber and another side is left to freely swing under gravity and external forces. This 3D membrane is modelled as the 2D system, considering only the plane of the main oscillation. It is perpendicular to the plane of the membrane itself. The first lump mass is defined as origin axis at the pivot point and the same position of the centre of the first lump mass.

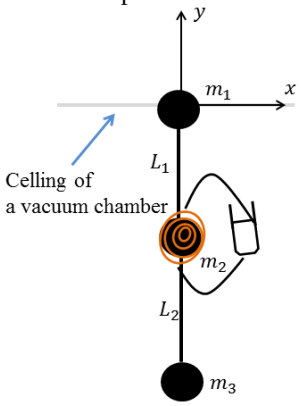

a)

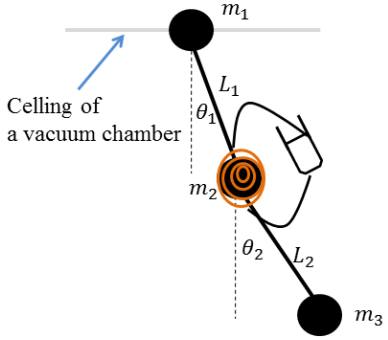

b

Fig 1 Multibody model of the three lump masses a) initial position b) Displacement after applying an external force

In order to solve the dynamics, we start using simple trigonometry to express the positions $x_1, y_1, x_2, y_2, x_3, y_3$ in term of the angles (θ_1 , θ_2) as:

$$x_1 = 0 \qquad [1]$$

$$y_1 = 0 \quad [2]$$

$$x_2 = L_1 \sin\theta_1 \quad [3]$$

$$y_2 = -L_1 \cos\theta_1 \quad [4]$$

$$x_3 = x_2 + L_2 \sin\theta_2 \quad [5]$$

$$y_3 = y_2 - L_2 \cos\theta_2 \quad [6]$$

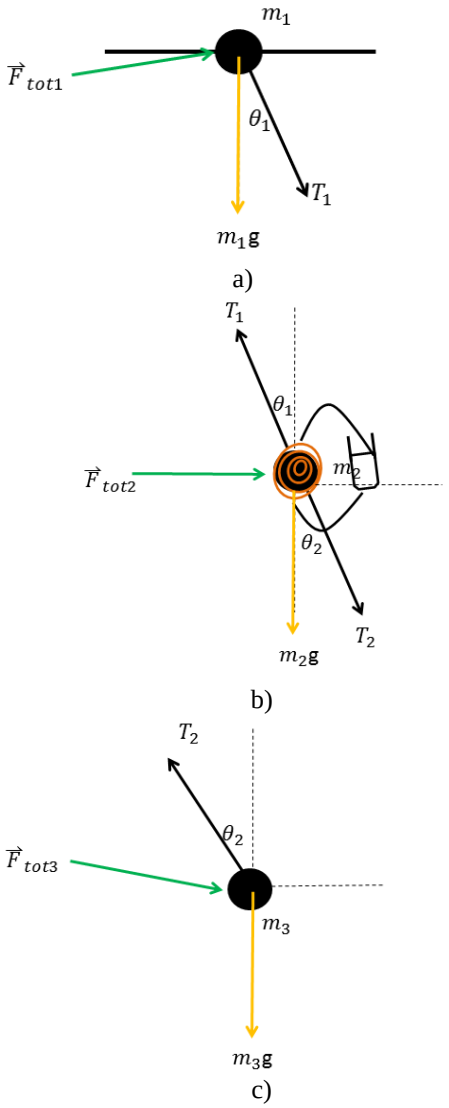

Fig 2 Free body diagram of each lump mass a) 1st lump mass b) 2nd lump mass c) 3rd lump mass

The free-body diagram in Fig 2 shows the net force acting on each mass. The net forces on the 1st mass are zero due to the pivot point. The dynamic equations of the 2nd lump mass are expressed to separate for the horizontal and vertical forces ($\vec{F}_{tot,i} = \vec{F}_{x\_tot,i} + \vec{F}_{y\_tot,i}$). Using the second law of Newton yields:

$$m_2\ddot{x}_2 = -T_1 s_1 + T_2 s_2 + F_{x\_tot,2} \quad [7]$$

$$m_2\ddot{y}_2 = T_1 c_1 - T_2 c_2 - m_2 g + F_{y\_tot,2} \quad [8]$$

Where m_i is the i[th] lump mass (i = 1, 2 and 3), $F_{k\_tot,i}$ is total force vector acting on the i^{th} lump mass in k direction. ($F_{k\_tot,i} = F_{\text{int},i} + F_{ext,i}$), $F_{\text{int},i}$ is the internal force from the rotational damper and spring ($F_{\text{int},i} = F_{spring} + F_{damper}$), $F_{ext,i}$ is the external force, $\vec{T}_j$ is the tension force generated by the rods (j = 1 and 2), $\ddot{x}_i$ is the x axis acceleration direction, $\ddot{y}_i$ is the y axis acceleration direction and $s_1 = \sin\theta_1, c_1 = \cos\theta_1$, $s_2 = \sin\theta_2, c_2 = \cos\theta_2$. The rotational spring and damper force are expressed as:

$$F_{spring} = K_{eq}(\theta_2 - \theta_1)/L_i \quad [9]$$

$$F_{damper} = C_{eq}(\dot{\theta}_2 - \dot{\theta}_1)/L_i \quad [10]$$

Where K_{eq} is equivalent stiffness and C_{eq} is equivalent damping coefficient. For the 3rd lump mass, it can be expressed as following:

$$m_3\ddot{x}_3 = -T_2 s_2 + F_{x\_tot,3} \quad [11]$$

$$m_3\ddot{y}_3 = T_2 c_2 - m_3 g - F_{y\_tot,3} \quad [12]$$

Then, we substitute Eq. [11] and [12] into Eq. [7] and [8] yields:

$$m_2\ddot{x}_2 = -T_1 s_1 - m_3\ddot{x}_3 + F_{x\_tot,3} + F_{x\_tot,2} \quad [13]$$

$$m_2\ddot{y}_2 = T_1 c_1 - m_3\ddot{y}_3 - m_3 g - m_2 g + F_{y\_tot,2} + F_{y\_tot,3} \quad [14]$$

We multiply $\cos\theta_1$ in Eq.[13] and $\sin\theta_1$ in Eq.[14] ,and rearrange the LHS in term of $T_1 s_1 c_1$:

$$T_1 s_1 c_1 = -c_1 m_2\ddot{x}_2 - m_3\ddot{x}_3 c_1 + c_1(F_{x\_tot,2} + F_{x\_tot,3}) \quad [15]$$

$$T_1 s_1 c_1 = s_1 m_2\ddot{y}_2 + s_1 m_3\ddot{y}_3 - s_1(-m_3 g - m_2 g + F_{y\_tot,2} + F_{y\_tot,3}) \quad [16]$$

Then,

$$c_1(F_{x\_tot,2} + F_{x\_tot,3}) - c_1 m_2\ddot{x}_2 - m_3\ddot{x}_3 c_1 = s_1 m_2\ddot{y}_2 + s_1 m_3\ddot{y}_3 - s_1(-m_3 g - m_2 g + F_{y\_tot,2} + F_{y\_tot,3}) \quad [17]$$

In order to find expressions for $\ddot{\theta}_1$ and $\ddot{\theta}_2$ in terms of θ_1, $\dot{\theta}_1$, θ_2, $\dot{\theta}_2$, the second derivatives of Eq. [3] -[6] are the acceleration as:

$$\ddot{x}_2 = -\dot{\theta}_1^2 L_1 \sin\theta_1 + \ddot{\theta}_1 L_1 \cos\theta_1 \quad [18]$$

$$\ddot{y}_2 = \dot{\theta}_1^2 L_1 \cos\theta_1 + \ddot{\theta}_1 L_1 \sin\theta_1 \quad [19]$$

$$\ddot{x}_3 = \ddot{x}_2 - \dot{\theta}_2^2 L_2 \sin\theta_2 + \ddot{\theta}_2 L_2 \cos\theta_2 \quad [20]$$

$$\ddot{y}_3 = \ddot{y}_2 + \dot{\theta}_2^2 L_2 \cos\theta_2 + \ddot{\theta}_2 L_2 \sin\theta_2 \quad [21]$$

The next step is a substitution of the acceleration from Eq. [18] to [21] in Eq. [17] for their angular expressions, and put these expressions in differential form:

$$\ddot{\theta}_1 L_1(m_2+m_3)+\ddot{\theta}_2 L_2 m_3\cos(\theta_2-\theta_1)-\dot{\theta}_2^2 L_2 m_3\sin(\theta_2-\theta_1) \quad [22]$$
$$= c_1(F_{x\_tot,2}+F_{x\_tot,3})$$
$$+ s_1(-m_3 g - m_2 g + F_{y\_tot,2}+F_{y\_tot,3})$$

In the same way for the 3rd lump mass, we multiply Eq. [11] by $\cos\theta_2$ and Eq. [12] by $\sin\theta_2$ and substitute the acceleration from Eq.[18] to [21]. It will be expressed as:

$$\ddot{\theta}_1 L_1 m_3\cos(\theta_2-\theta_1)+\ddot{\theta}_2 L_2 m_3+\dot{\theta}_2^2 L_1 m_3\sin(\theta_2-\theta_1) \quad [23]$$
$$= s_2(m_3 g + F_{y\_tot,3}) - c_2 F_{x\_tot,3}$$

Eq. [22] and [23] can be written in matrix form:

$$\begin{bmatrix} C_1 & C_2 \\ C_3 & C_4 \end{bmatrix}\begin{bmatrix} \ddot{\theta}_1 \\ \ddot{\theta}_2 \end{bmatrix}=\begin{bmatrix} A_1 \\ A_2 \end{bmatrix} \quad [24]$$

Where:

$$C_1 = (m_2+m_3)L_1$$
$$C_2 = m_3 L_2\cos(\theta_2-\theta_1)$$
$$C_3 = m_3 L_2\cos(\theta_2-\theta_1)$$
$$C_4 = m_3 L_2$$
$$A_1 = \dot{\theta}_2^2 L_2 m_3\sin(\theta_2-\theta_1)+c_1(F_{x\_tot,2}+F_{x\_tot,3})$$
$$+s_1(F_{y\_tot,2}+F_{y\_tot,3}-(m_2+m_3)g)$$
$$A_2 = -\dot{\theta}_2^2 L_1 m_3\sin(\theta_2-\theta_1)+s_2(m_3 g+F_{x\_tot,3})-c_2 F_{x\_tot,3}$$

Then, we multiply the inverse of LHS matrix (C matrix). The angular accelerations of both angles are calculated as:

$$\begin{bmatrix} \ddot{\theta}_1 \\ \ddot{\theta}_2 \end{bmatrix}=\begin{bmatrix} C_1 & C_2 \\ C_3 & C_4 \end{bmatrix}^{-1}\begin{bmatrix} A_1 \\ A_2 \end{bmatrix} \quad [25]$$

A Kapton 1 mil (0.05 x 0.20 m^2) model in Fig 3 is tested by applying the forces (0.1 mN) on the 2nd and 3rd masses for 2 seconds In this test, we assume that C_{eq} and K_{eq} are 0.05 $N\cdot m/rad$ and 0.0004 $N\cdot m\cdot s/rad$ respectively. The result in Fig 3 shows the displacement of third lump mass in x direction equal to 0.0254 m.

III. UNDERDAMPED FREE VIBRATION

A free vibration maintains the same amplitude. In reality, the amplitude of oscillation of the membrane under consideration continuously decreases due to friction. The damping ratio (ξ) can be induced by external and internal factors. External damping is generated by the existence in the system of external, non-conservative forces applied (e.g. air friction) while the internal damping depends on material characteristics. In this study, we, therefore, aim to measure the amplitude decay of displacement to determine the damping ratio of the material and natural frequency from their frequency domains.

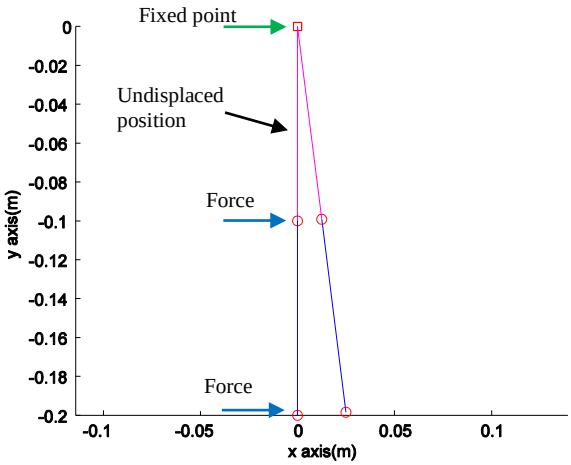

Fig 3 Multibody simulation of Kapton 1 mil is applied with application of 0.1 mN for 2 seconds

With low bending stiffness of the multilayer insulation membrane, air drag can have a substantial effect on the damping. The experiment is, therefore, set up in a vacuum chamber. The suitable generalized coordinates of the dynamic system in Fig 1 are defined by θ_1 and θ_2. Based on an unforced damped second degree of freedom, an oscillation dynamic equation is written as following:

$$M\ddot{\theta}+C\dot{\theta}+K\theta=0 \quad [26]$$

Where M is mass matrix, C is the damping coefficient matrix, K is the stiffness matrix, $\ddot{\theta}$ is angular acceleration matrix [$\ddot{\theta}_1$, $\ddot{\theta}_2$], $\dot{\theta}$ is angular velocity matrix [$\dot{\theta}_1$, $\dot{\theta}_2$] and θ is angular matrix [θ_1, θ_2].

It is well known that when the free vibration response is affected by non-conservative forces, amplitude gradually decreases as shown in Fig 4.

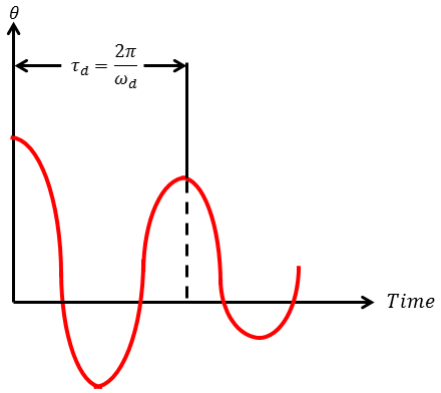

Fig 4 Transient response of a decaying time-history

The damped vibration period in Fig 4 is defined as:

$$\tau_d = \frac{2\pi}{\omega_d} \quad [27]$$

Where ω_d = damped natural angular frequency $\omega_d = \sqrt{1-\xi^2}\,\omega_n$

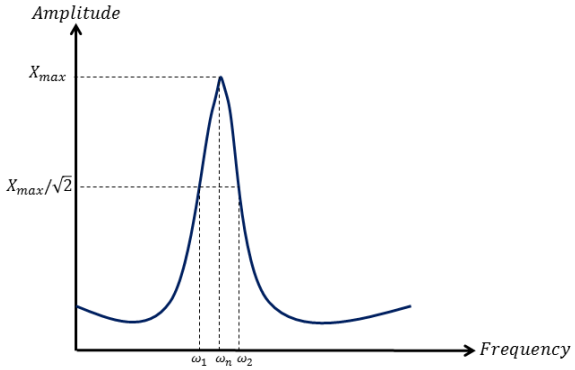

Fig 5 Frequency response

In order to estimate a damping ratio (ξ) of a sample by calculating from frequency domain, the half-power bandwidth method (Fig 5) is very useful tool for computing the damping ratios for multi degree freedom systems as:

$$\xi = \frac{(\omega_2 - \omega_1)}{2\omega_n} \quad [28]$$

From the amplitude decay and frequency response in Fig 4 and Fig 5, we can find an equivalent stiffness constant (K_{eq}), and equivalent damping coefficient (C_{eq}). They are defined as:

$$K_{eq} = \omega_n^2 M_{tot} \quad [29]$$

And

$$C_{eq} = 2M_{tot}\omega_n\xi \quad [30]$$

Where M_{tot} is a total mass of a sample.

III.I Normal modes

In order to analyse the normal modes of multibody model, we reduce Eq. [26] with non-proportional damping to a standard eigenvalue form. It can be written as:

$$M\ddot{\theta} + K\theta = 0 \quad [31]$$

And general solutions are expressed as $\theta_{1,2}(t) = A_{1,2}e^{j\omega t}$. Therefore, we can find the normal mode as:

$$\det(K - \omega^2 M) = 0 \quad [32]$$

The model of this study consists of the three lumps and each of them is connected with rigid rods. This dynamics is similar to the dynamics of double pendulums. As following Rafat [18], the natural frequencies or normal modes of oscillation, the eigenvalues (ω^2) of the multibody model are determined by solving Eq. [32] and are given by the solution of quadratic as:

$$\omega_{\pm}^2 = \frac{k_1k_4 + k_2k_5 \pm \sqrt{(k_1k_4 - k_2k_5)^2 + 2k_1k_5k_6^2}}{2\left(k_2k_4 - k_6^2\right)} \quad [33]$$

Where

$$k_1 = g(m_{rod,2}L_1 + m_{rod,1}L_1/2)$$
$$k_2 = I_1 + m_{rod,1}L_1^2 + m_{rod,1}(L_1/2)^2$$
$$k_4 = m_{rod,2}(L_1/2_1)^2 + I_2$$
$$k_5 = -m_{rod,2}g(L_1/2)$$
$$k_6 = -L_1 m_{rod,2}(L_1/2)$$

I_1 and I_2 are the moments of inertia of rigid rod

From Eq.[33], we can find the normal mode of the oscillation. The ratios of amplitude factors A_1 and A_2 of two coordinates are expressed as:

$$\left(\frac{A_1}{A_2}\right)_{\pm} = \frac{-k_5k_6}{\omega_{\pm}^2\left(k_2k_4 - k_6^2\right) - k_1k_4} \quad [34]$$

The 1st mode ($(A_1/A_2)_+ > 0$) presents that both rigid rods oscillate in the same direction (in-phrase in Fig 6(a)). The 2nd mode($(A_1/A_2)_- < 0$) shows that rigid rods move in opposite directions. (out of phrase in Fig 6(b))

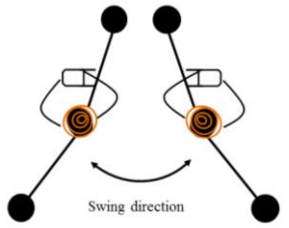

a)

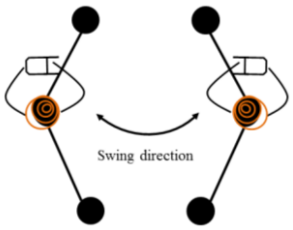

b)

Fig 6 Two normal modes of multibody model
a) 1st mode (slow mode) b) 2nd mode(fast mode)

III.II Object tracking

In order to measure the motion of MLI inside a vacuum chamber during the experiment, object motion tracking, through a sequence of still photos, is used to measure the movement of each lump mass. Three red marks on the specimen (Fig 8 (a)), representing each lump mass, are required to measure their movements.

There are five major steps in the process (Fig 7). It starts to be given an image sequence from a static camera (Fig 8 (a)). The next step, the extraction of each red component is to discriminate each red point from others (Fig 8 (b)). In this step, the camera noise is filtered. In recognition and representative process (Fig 8 (c)), extracted red pixels are converted as binary image and then we use the results of the recognition to process a representation of each recognized tracked object. The last step, object tracking, uses the Kalman filter [19, 20] to estimate an observable state, which is updated in each time step with a linear state update and plot the tracking blue rectangle around the object's movement at each time step (Fig 8 (d)).

III.II Kalman filter

The purpose of a Kalman filter is to predict a state and use measurements to correct the prediction.

III.II.I Prediction

Discrete-time Kalman filters begin each iteration by predicting the process's state using a linear dynamics model.

1) State prediction, $\bar{X}_{i+1}$*:* a Kalman filter make a prediction of the state at i and state covariance prediction, $\bar{P}_{i+1}$, are defined by:

$$\bar{X}_{i+1} = \Phi_s \hat{X}_i \quad [35]$$

Where Φ_s is the error state transition matrix.

2) State covariance prediction: a Kalman filter estimate error covariance $\bar{P}_{i+1}$ forward one time step:

$$\bar{P}_{i+1} = \Phi \bar{P}_{i+1} \Phi^T + Q \quad [36]$$

Where Q is process noise covariance.

III.II.II Measurement update

After predicting the state and its error covariance at time i using the time update steps, a Kalman filter during the measurement updates steps.

1) Kalman Gain: the Kalman filter computes a Kalman gain K_i used to correct the state estimate $\bar{X}_{i+1}$:the state estimate $\bar{X}_{i+1}$:

$$K_i = \bar{P}_{i+1} H_{i+1}^T (H_{i+1} \bar{P}_{i+1} H_{i+1}^T + R)^{-1} \quad [37]$$

Where H_{i+1} is a matrix to convert state space into measurement space, and R is a measurement noise covariance.

2) *Update Estimate with measurement* $\hat{X}_{i+1}$: Kalman gain and measurement from time step, we can update the state estimate.

$$\hat{X}_{i+1} = \bar{X}_{i+1} + K_{i+1}[X_i - H_{i+1} \bar{X}_{i+1}] \quad [38]$$

3) *Error Covariance estimate*: The final step of the Kalman filter's iteration is to update the error covariance $\bar{P}_{i+1}$ to $\hat{P}_{i+1}$.

$$\hat{P}_{i+1} = [I - K_{i+1} H_{i+1}] \bar{P}_{i+1} \quad [39]$$

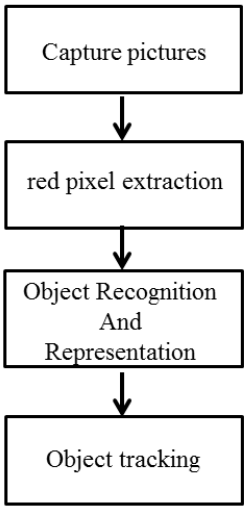

Fig 7 Object tracking process

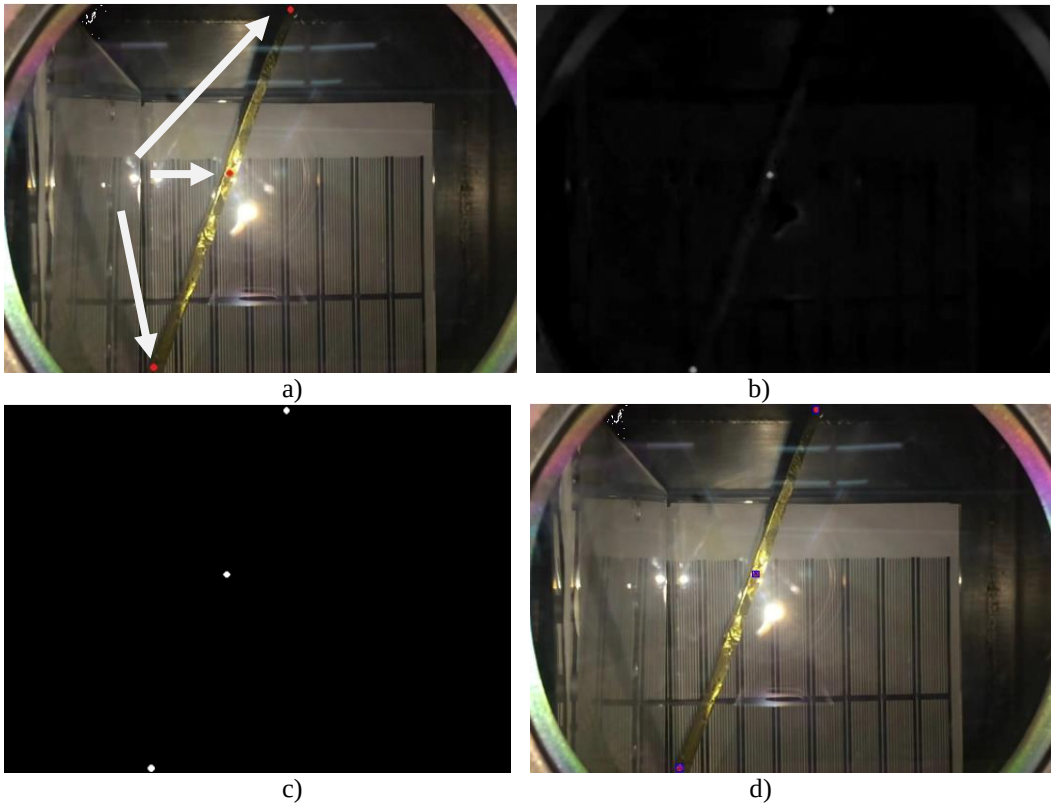

Fig 8 Object tracking simulation a) an extracted image from a video record b) Extracting the red component from a picture c) Converting a grayscale image into a binary image d) Blue mark on the red three points on an image

.

III.III Radiation pressure force of the spotlight

The forced motion investigation is the experiment to measure the motion of the free end of a membrane by exposing the radiation force from spotlight representing the solar radiation force.

The spotlight is assumed to be a perfect parabolic mirror around the light source[21]. The estimation of the radiation pressure can be calculated as:

$$I_{rad} = \frac{2P\varepsilon}{4\pi d^2} \quad [40]$$

Where I_{rad} is flux of radiation (W/m^2), P is the power of the spotlight, d is the distance from the light source to the membrane (m) and ε is an transmissivity efficiency of the glass window of the vacuum chamber, which approximates as perfect (ε =1).

In this study, the specular and diffuse reflection properties of MLI are considered. Therefore, solar radiation force ($\vec{F}_{\exp}$) [22] can be calculated as:

$$\vec{F}_{\exp} = \frac{I_{rad}}{c_{light}} A_{\exp} \cos(\theta_{inc}) \left\{ 2\left(\frac{C_{Rd}}{3} + C_{Rs} \cos(\theta_{inc}) \right) \vec{n} + (1 - C_{Rs}) \vec{s} \right\} \quad [41]$$

Where $A_{\exp}$ is exposed area of sample, c_{light} is the speed of light (299,792,458 m/s), C_{Rd} and C_{Rs} are the coefficients of diffuse and specular respectively. The relationship in C_{Rs} , C_{Ra} and C_{Rd} is 1 = C_{Rs} + C_{Ra} + C_{Rd} . The surface normal unit vector, $\vec{n}$, and the spotlight incidence vector, $\vec{s}$. In this experiment, the light is exposed in x axis direction and an incident angle, θ_{inc} is perpendicular to a membrane.

Then, Eq. [41] is used as external force acting on multibody model to investigate the forced motion.

IV EXPERIMENTAL SETUP

Both schematic diagrams of free motion and forced motion setups are shown in Fig 9 and Fig 10 respectively. There are three samples chosen for this experiment: PET 1 mil, Kapton 1 mil and PET 5 mils. All samples have the same width and length of 0.05 x 0.20 m^2. Basically, each sample is a one substrate layer and coated with extremely thin aluminium (1000 Å). PET is coated on both sides while Kapton is coated on one side and their characteristics and reflection properties as shown in Table 1.

The free motion setup in Fig 9 aims to find the damping characteristics of each specimen. A sample is

attached with a stand and held by an electromagnetic latch. The camera (Canon IXUS 110 IS, 30fps) is set in front of the mirror. Fig 11 shows the amplitude decrement of Kapton 1 mil in the normal atmosphere that is remarkably different with the test in vacuum environment (Fig 15(b)). Before starting the experiment, we drain the air inside of the vacuum chamber down to 10^{-4} mbar (high vacuum level). Next, we turn off the power to the electromagnetic latch to release the sample, swinging freely and recording a video by the camera. The data are applied with the object tracking process in Fig 7 to measure the amplitude decay of both θ_1 and θ_2, and apply FFT process to define their natural frequencies.

For the forced motion set up in Fig 10, we use the high power spotlight (2000 W) for exposure on a sample and use a dimmer to vary the spotlight power to study the relationship between light intensity and resulting displacements. The high resolution laser measurement of Model optoNCDT 1700-2LL [23], which is a special laser sensor for lustrous metals, high resolution: 0.1µm and measuring range 2 mm, is used to measure the displacement at the bottom of sample (the 3rd lump mass) as shown in Fig 10(c). In order to interface sensor with laptop, we use a RS422 converter [23], which converts serial data from the sensor to the USB line.

In addition, the results of both experiments will be compared with the displacement from an analytic solution of both multibody dynamics and finite element method (through commercial package ANSYS®).

Table 1 Properties of PET and Kapton [16, 17]

Material type	Thickness mil (µm)	Mass (mg)	Density (kg/ m^3)	Young's Modulus (N/m^2)	*Cs, Cd, Ca*
PET 1mil	1(25.4)	0.3530	1,390	$8.81\text{x}10^9$	0.60 0.26 0.14
PET 5 mils	5(127)	1.7653	1,390	$8.81\text{x}10^9$	0.60 0.26 0.14
Kapton 1 mil	1(25.4)	0.3606	1,420	$2.50\text{x}10^9$	0.60 0.26 0.14

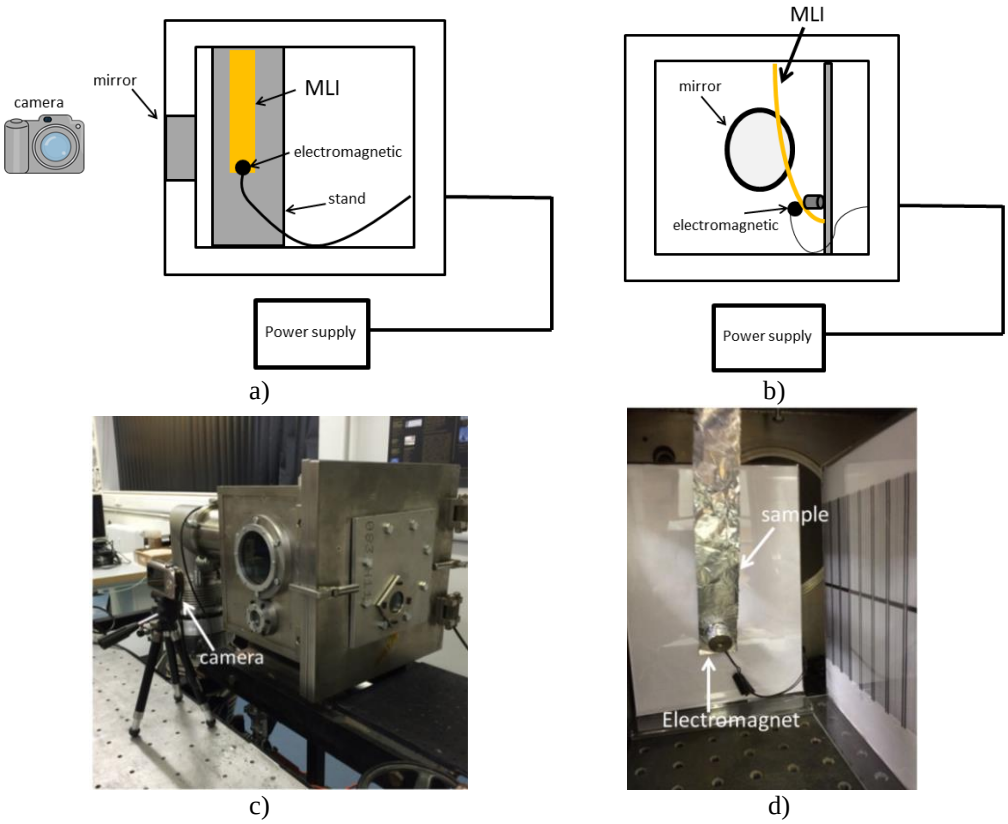

Fig 9 Schematic drawing and experimental setup of the free motion setup a) schematic on side view b) schematic on backside view c) outside vacuum d) inside vacuum

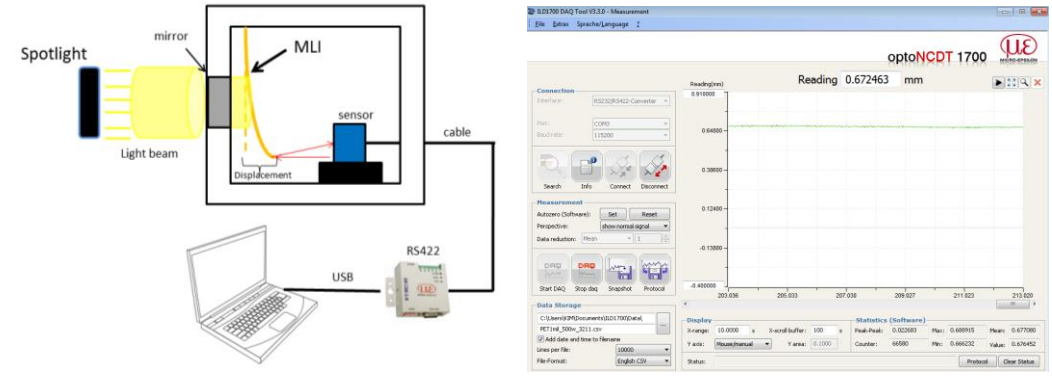

Fig 10 Schematic drawing and experimental set up of a forced motion setup a) schematic on side view b) interface program c) outside view of the experiment d) inside view of an vacuum

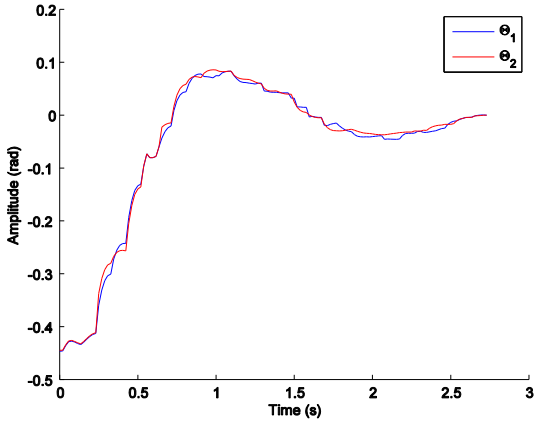

Fig 11 Free vibration response of kapton 1 mil in normal atmophere

V EXPERIMENTAL RESULTS

V.I Free motion investigation.

The results of object tracking detection of the free fall vibration of PET 1 mil, Kapton 1 mil and PET 5 mils are shown as in Fig 12, Fig 13 and Fig 14 respectively. The red component's movements are marked by a blue rectangular. Their natural frequencies obtained from the experimental results and multibody simulations have been verified by performing with ANSYS® (commercial FEA package).

Fig 15 shows the free vibration of both θ_1 and θ_2 including the natural frequency of each sample by processing with Fast Fourier Transform (FFT). The natural frequencies of both θ_1 and θ_2 are 0.5156, 0.2109 and 1.3090 Hz of PET 1 mil, Kapton 1 mil and PET 5 mils respectively.

From these results, we can compute damping ratio (ξ) from Eq. [28]. The equivalent rotational spring and damping coefficients on the 2nd lump mass can be calculated from Eq.[29] and [30] respectively as shown in Table 2. We apply these data in the multibody model to investigate their amplitude decays and natural frequencies.

Table 2 stiffness and damping coefficients of MLI samples

Material	ξ	K_{eq} ($N \cdot m / rad$)	C_{eq} ($N \cdot m \cdot s / rad$)
PET 1 mil	0.0409	0.0258	2.467E-04
Kapton 1mil	0.0441	0.0251	2.652E-04
PET 5 mils	0.0145	0.1162	4.153E-04

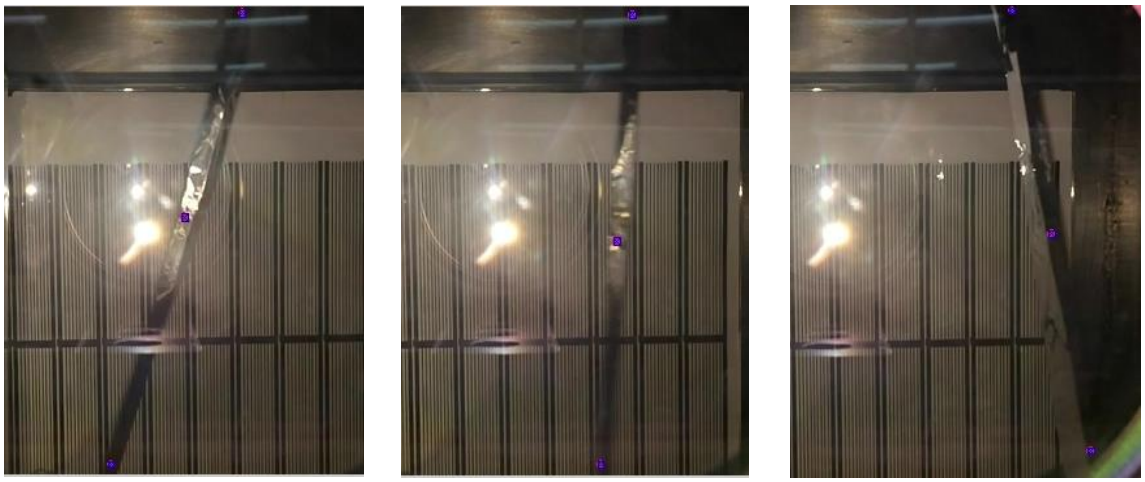

a) b) c)

Fig 12 Detection red components of PET 1 mil

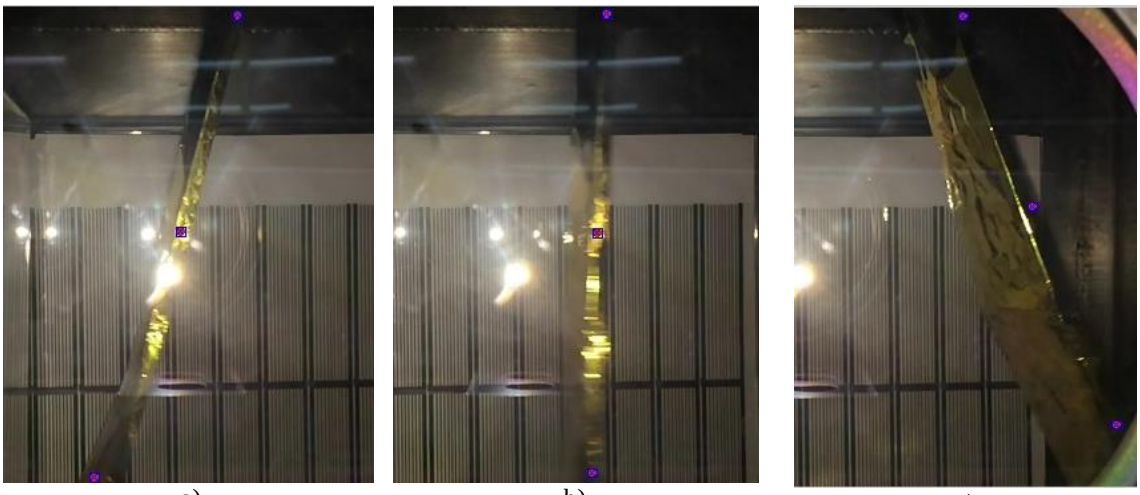

a) b) c)

Fig 13 Detection red components of Kapton 1 mil

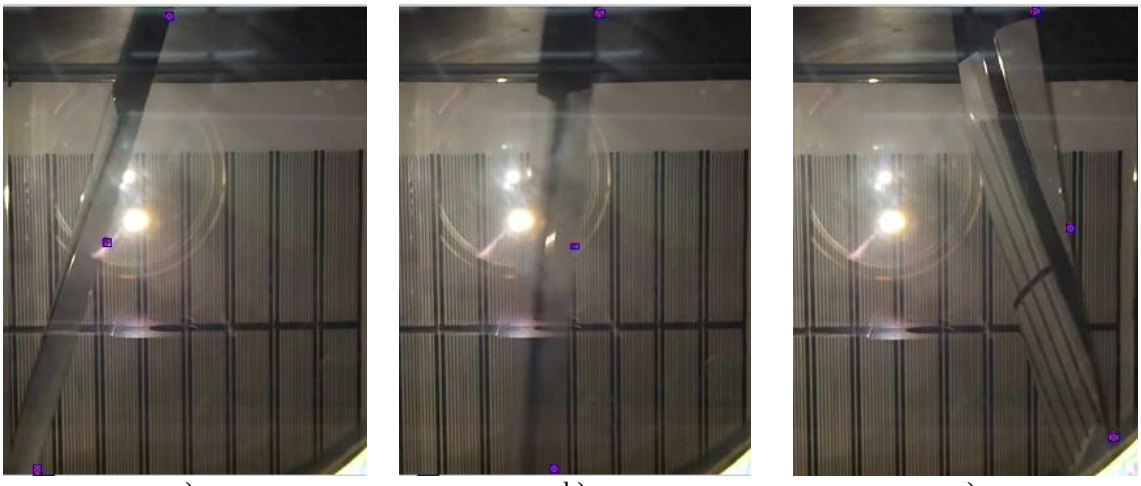

a) b) c)

Fig 14 Detection red components of PET 5 mils

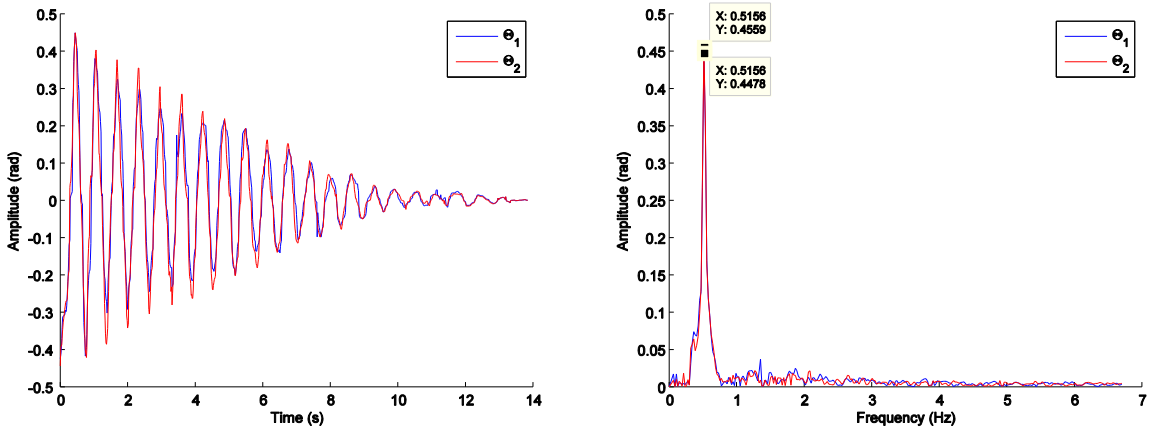

a)

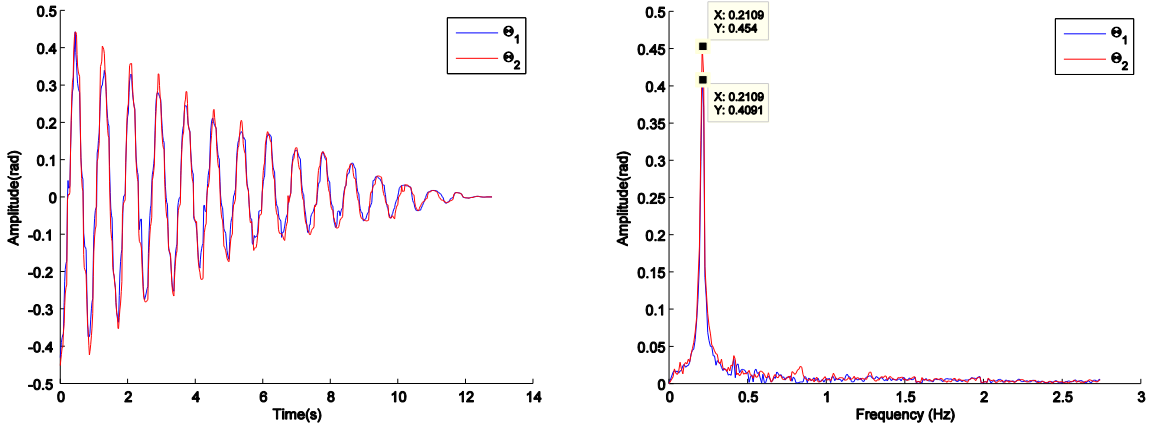

b)

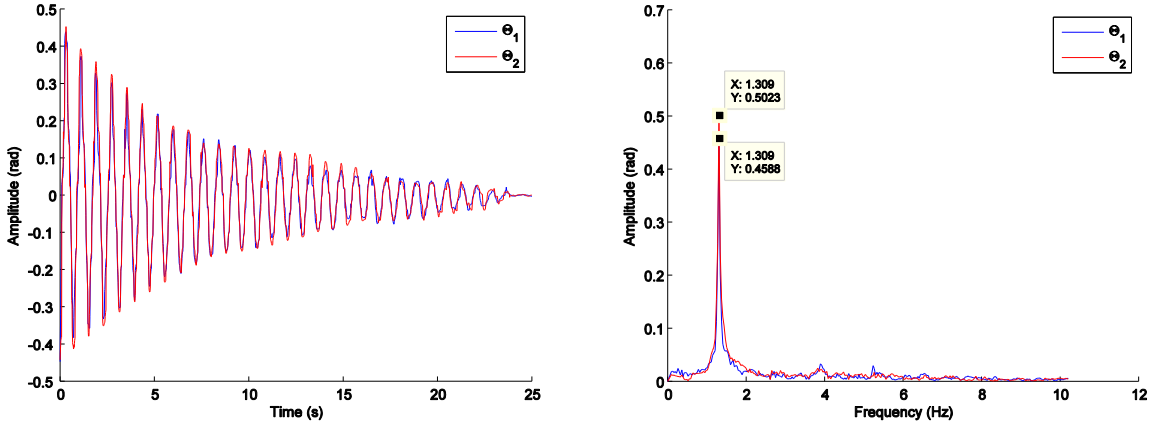

c)

Fig 15 Free vibration response of the damping experiments in time and frequency domains a) PET 1 mil b) Kapton 1 mil c) PET 5 mils

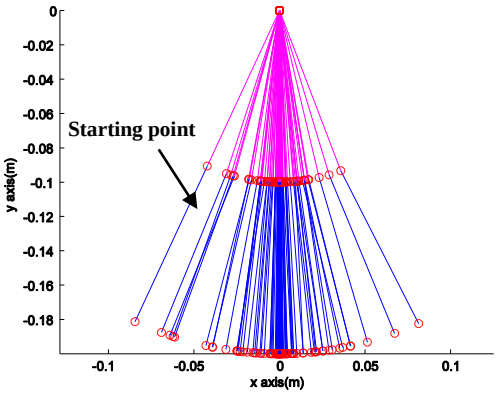

Fig 16 Free swinging of multibody dynamics model

The free motion of the multibody simulation of PET 1 mil shows in Fig 16. The modal analysis of ANSYS for the 1st mode and 2nd mode of PET 1mil shows in Fig 17. Fig 18 indicates that the free vibration responses (θ_1 and θ_2) of multibody model in each sample. Kapton 1 mil is the fastest to settle into its equilibrium position while PET 5 mils take the longest time. This is due to their damping ratios (ξ). Kapton 1 mil and PET 5 mils have the highest and lowest damping coefficient (C_{eq}) respectively. Comparing the experimental results with the results of the multibody simulations, the early period of amplitude peak of both matches well after passing 2-3 periods and then both phrases and amplitudes of experimental results gradually shift and decrease faster than the simulation results of multibody model. It can explain that although the air pressure inside a vacuum chamber (10^{-4} mbar) is extremely low, a low amount of air significantly obstructs its motion including hinge frictions.

Comparison the absolute amplitude θ_1 and θ_2, the absolute values of θ_1 in both the experimental results and the simulation of multibody model in all samples in Fig 15 and Fig 18 respectively are lower than the absolute values of θ_2 until almost the end period of oscillation but both θ_1 and θ_2 are inphase over oscillation period. These results, therefore, interpret like the 1st mode as shown in Fig 19 that the expandable results of the vibration response of PET 1 mils.

The natural frequencies of the PET 1 mil, Kapton 1 mil and PET 5 mils from the experimental results in Fig 15 are 0.5156, 0.2109 and 1.3090 Hz that coherent well the natural frequency determined by multibody simulation in Fig 18 (0.5581, 0.2087 and 1.4190 Hz respectively). As the results of the vibration response both time domain and frequency domain, these results correlate as the 1st mode response.

Comparing the experimental results with analytic theory (normal mode) and FEA as shown in Table 3, The natural frequency of normal modes and FEA (ANSYS®) of PET 1mil, Kapton 1mil and PET 5 mils match well in the 1st mode of normal modes (0.5265, 0.2299 and 1.3480 Hz) and ANSYS® (0.5350, 0.2095 and 1.3338 Hz) respectively. Thus, the natural frequencies of the experimental results are good agreement in both analytic theory and FEA methods.

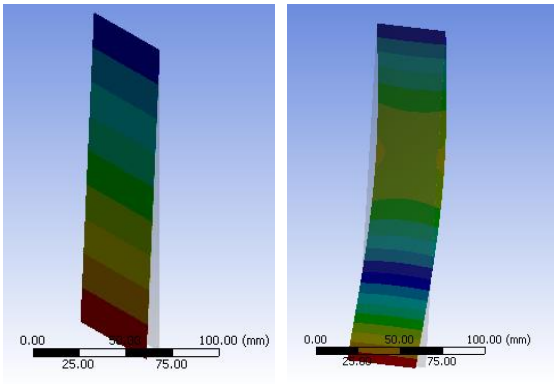

a) b)

Fig 17 Mode shape and the natural frequencies results of PET 1 mil from FEA(ANSYS®): Natural modes a) the 1st mode b) the 2nd mode

Table 3 Comparison the natural frequency of experimental results with multibody simulation and analytic methods (normal mode and FEA)

Material	Natural Frequency (Hz)					
	Free vibration simulation (MATLAB®)	Free vibration method (Experiment)	Normal mode (Theory)		Free vibration method (ANSYS®)	
	f_1	f_1	f_1	f_2	f_1	f_2
PET 1 mil	0.5581	0.5156	0.5265	1.3474	0.5350	1.3815
Kapton 1mil	0.2087	0.2109	0.2299	0.6147	0.2095	0.6270
PET 5 mils	1.4190	1.3090	1.3480	8.1566	1.3338	8.3209

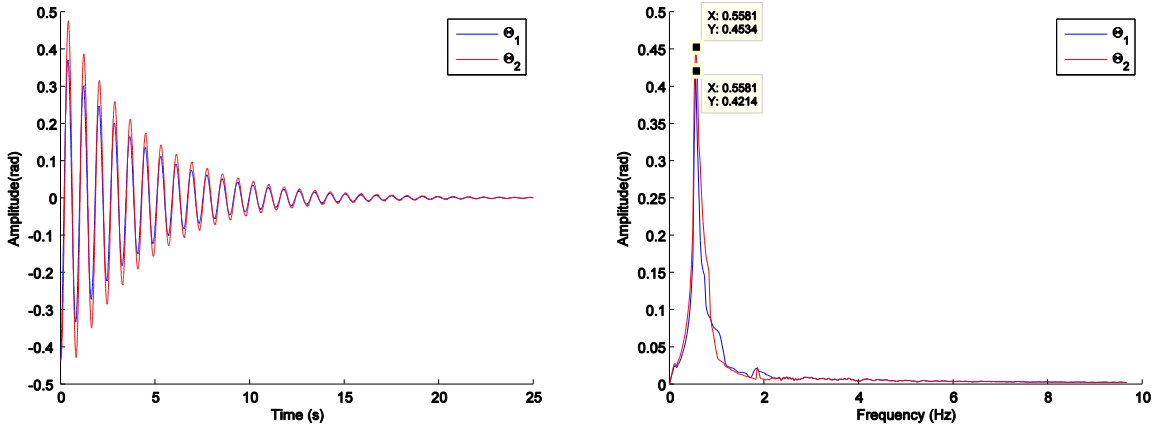

a)

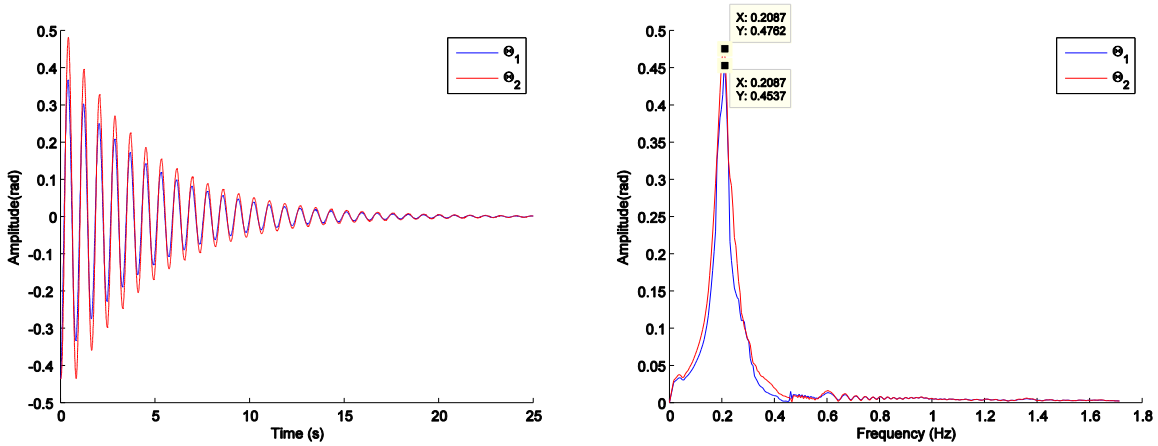

b)

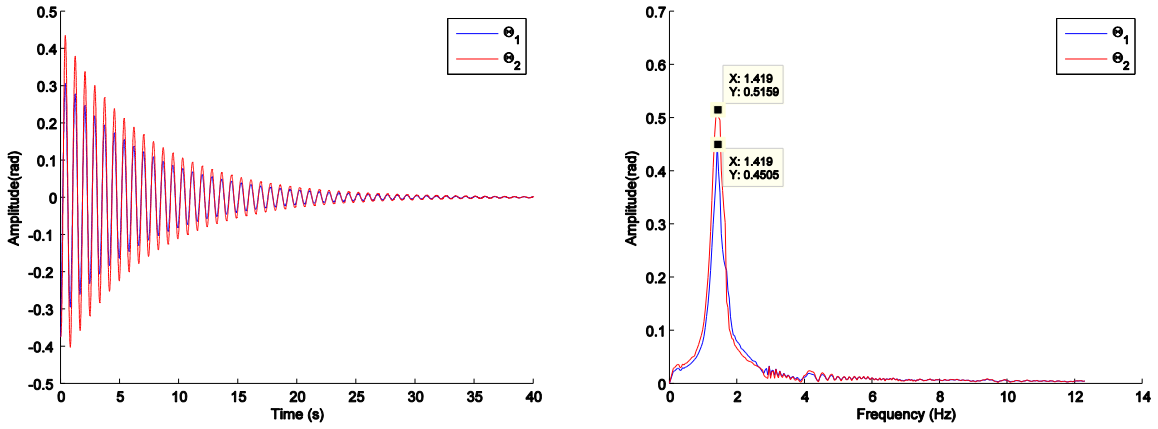

c)

Fig 18 Free vibration response of multibody model in time and frequency domains a) PET 1 mil b) Kapton 1 mil c) PET 5 mils

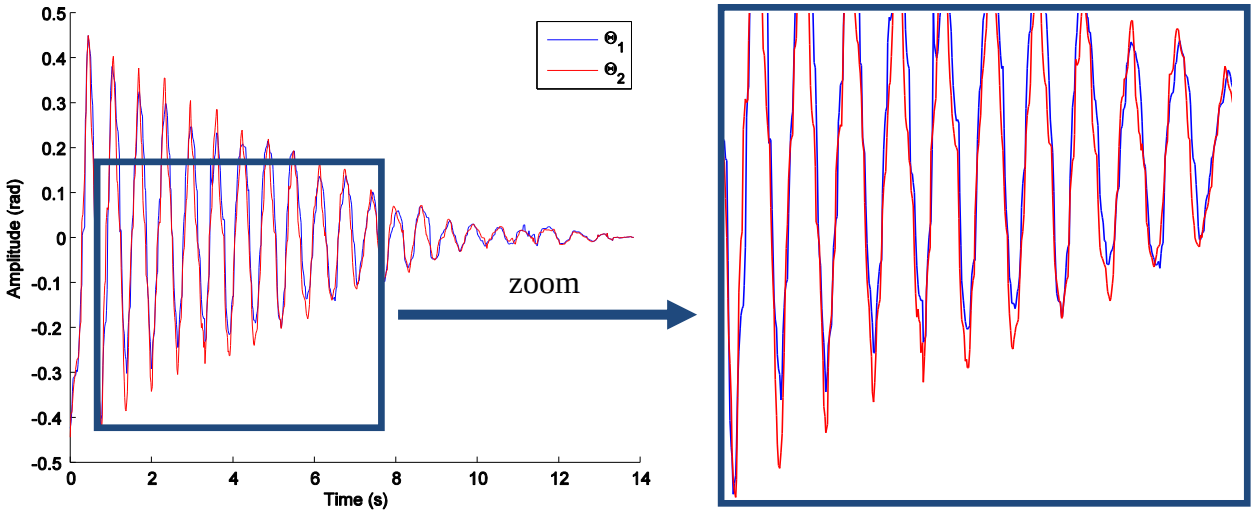

a)

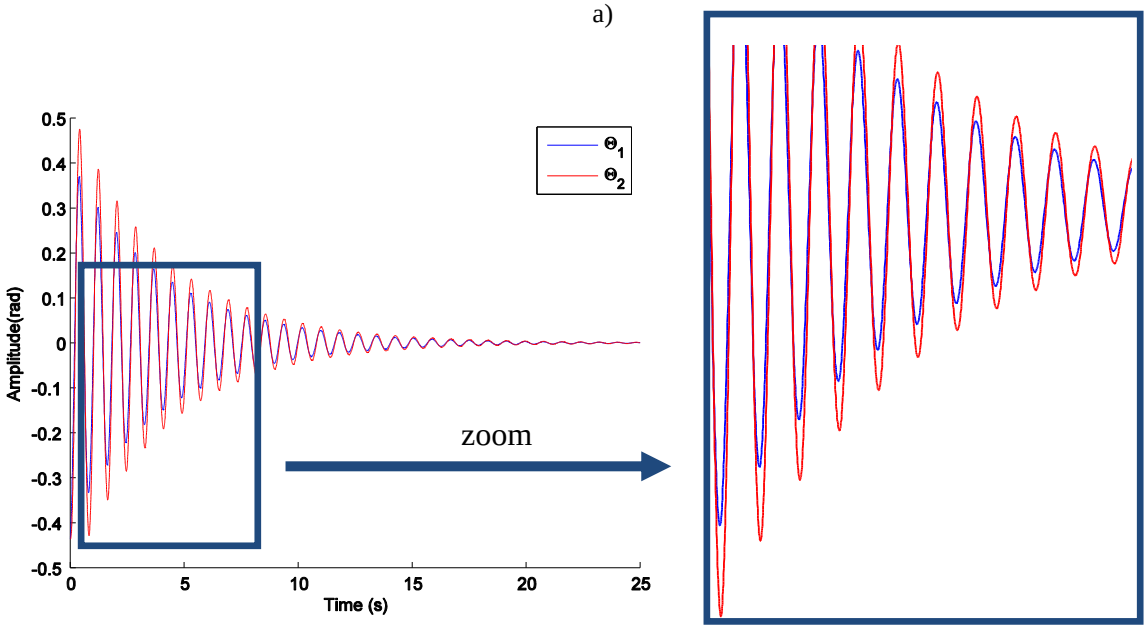

b

Fig 19 Expandable free vibration response of the experimental results with multibody model of PET 1 mil a) the experimental result b) the simulation of multibody model.

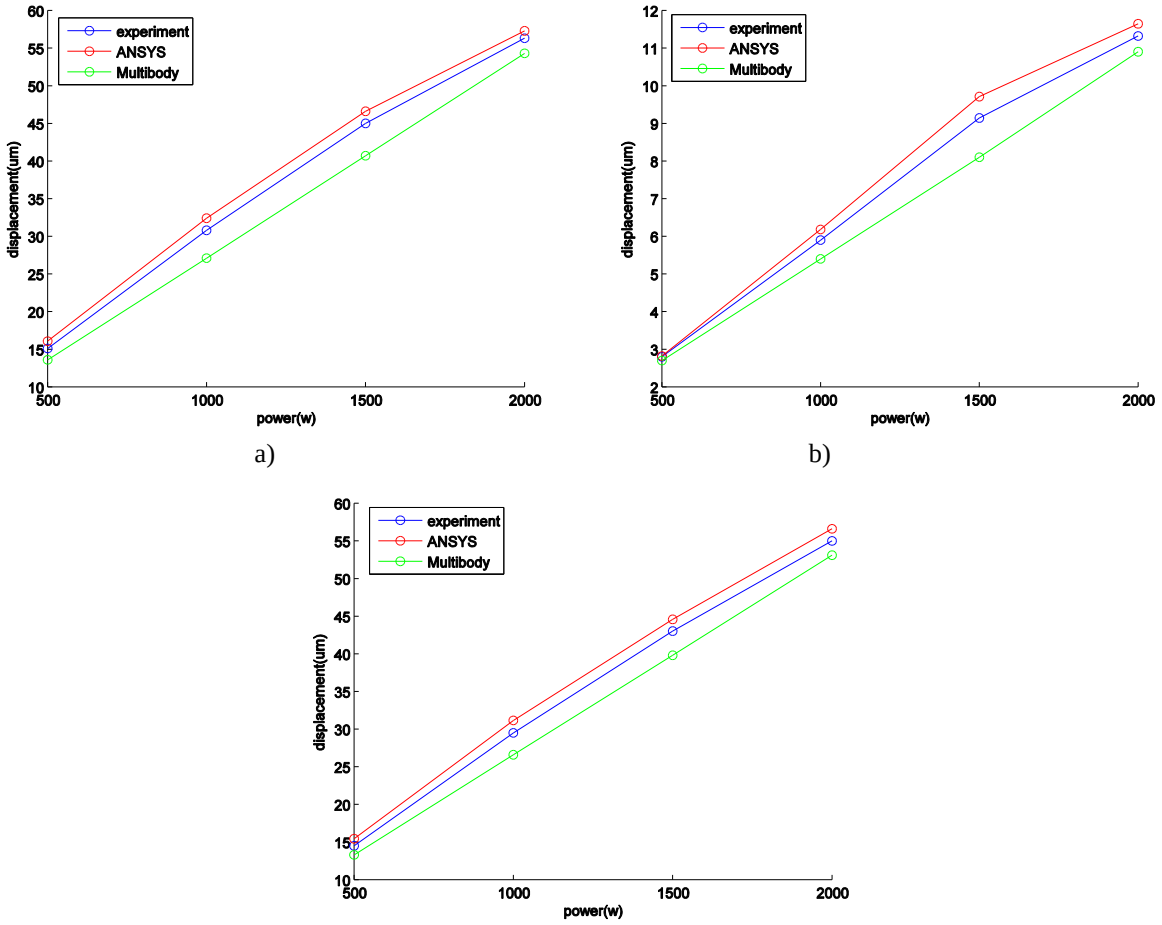

Fig 20 Comparison of displacement results of forced motion experiment, FEA and multibody dynamics a) PET 1 mil b) Kapton 1 mil c) PET 5 mils

Table 4 The relative error of the analytic simulation (Multibody model and FEA) compared to the measured displacement

Material	Method	Δ (%error)			
		500(w)	1000(w)	1500(w)	2000(w)
PET 1 mil	Multibody	-9.93	-12.01	-8.13	-3.55
	FEA	6.46	5.19	5.20	1.73
Kapton 1mil	Multibody	-8.28	-9.83	-7.48	-3.45
	FEA	6.48	5.59	5.62	2.90
PET 5 mils	Multibody	-3.57	-8.49	-11.40	-3.71
	FEA	0.70	4.75	6.20	2.88

V.II Forced motion investigation.

After observing the displacement on the third lump mass of experiment and both theoretical methods by varying the spotlight power (500, 1000, 1500 and 2000 W), Fig 20 shows that the experimental results match with multibody model and FEA. The displacement is very small in the order of micrometres. The displacement of multibody model (MATLAB®), green line (linear results), is lower than FEA and experiment (red and blue lines) that show non-linear results in all membrane types. The results of the comparison are shown in Fig 20.

In Table 4, Δ is the relative error of the deformation of both multibody and FEA model compared to the real measured displacement. The relative error of the multibody is maximum at 1000W while the relative error of FEA has the maximum relative error at 500W for both PET 1 mil and Kapton 1 mil but the relative minimum error is PET 5 mils. The relative error of both

multibody and FEA of all membrane types at 2000W is less than that at 1000W and 1500W for all cases but it is not for the relative error of FEA (PET 5 mils, $\Delta = 0.70$) at 500W.

In overall, the relative error range of multibody by varying the spotlight power is 3.45-12.01% but the relative percentage error range of FEA is around 0.70-6.48%. It is evident that finite element analysis tool is enable to solve a non-linear problem of behaviour of real structure better than multibody model. However, when coupled with the attitude and orbital dynamics propagation, its computational cost is large due to the several degrees of freedom. The relative error of the multibody model is insignificantly different to the relative error of FEA. It can, therefore, be approximated the deformation instead of the FEA model. It is able to be handled inside the propagation and cheaper numerical cost.

VI CONCLUSIONS

This paper presents the two experiment methods to validate the multibody model. The first experiment (free motion experiment) is carried out to measure damping characteristics of the membranes and their fundamental natural frequency. The last investigation is performed to study the forced motion of a membrane by exposing the radiation pressure force of a spotlight. Both experimental results and the simulations of multibody model are validated by analytic theory and finite element analysis (FEA).

The free motion experiment is effective to measure damping characteristic of a thin and low strength membrane. This method is able to determine the damping characteristics of each sample. The natural frequencies results obtained by using analytic methods (the natural frequency theory and FEA) have a good agreement with both the experimental results and simulations of the multibody model. The multibody model can be an effective simple model for this debris type if we can determine their internal damping characteristics. The experimental results of all samples, however, show that their amplitude decays are going to steady state faster than the results of the multibody model because the tiny amount of the air in a vacuum chamber and hinge friction significantly resists the motion of a sample.

The forced motion experiment of the multibody model is a fairly agreement with both the experimental and FEA results. The relative errors of FEA are coherent better than those of multibody model. It is due to FEA being able to better solve higher degree of freedom. In case of orbital prediction of the HAMR objects, it will, however, become more serious in enormous computational costs of a numerical propagation. The multibody model provides a cheaper cost to propagate the orbital dynamics of this debris type.

However, the forced motion investigation is required the high accuracy instruments, which are quite expensive. It is due to low strength of a membrane leading to deform simply. We cannot buy a temperature sensor and light detector due to the budget limitation. The thermal expansion of membrane due to the high power spotlight (2000w) mays causes the deformation on some parts of a membrane. The temperature sensor is, therefore, required to measure its temperature during experiments for the more accuracy displacement results of this investigation. The validation of the radiation pressure force equation (Eq.[41]) from the spotlight can be confirmed by a light detector measuring the actual power of the spotlight on a membrane comparing with the calculation of the equation.

ACKNOWLEDGEMENTS

This work was funded by Ministry of Science and Technology of the Thai government and the European Office of Aerospace Research and Development (project award FA8655-13-1-3028).

REFERENCES

1. Schildknecht, T., et al. *Color photometry and light curve observations of space debris in GEO*. in *Proceedings of Advanced Maui Optical and Space Surveillance Technologies Conference*. 2008. Maui Hawaii.
2. Früh, C. and T. Schildknecht, *Variation of Area-to-Mass-Ratio of HAMR Space Debris objects.* Monthly Notices of the Royal Astronomical Society, 2011. 419(4): p. 3521-3528.
3. Schildknecht, T., R. Musci, and T. Flohrer, *Properties of the high area-to-mass ratio space debris population at high altitudes.* Advances Space in Research, 2008. 41(5): p. 1039-1045.
4. Dever, J.A., et al., *Mechnical properties degradation of TEFLON FEP returned from the hubble space telescope*, in *36th Aerospace Sciences Meeting&Exhibit*. 1998.
5. Sen, L., et al., *A model to describe the size distribution of satellite breakup debris*, in *63rd International Astronautical Congress*. 2012: Naples, Italy.
6. Murakami, J., et al., *Micro-satellite impact tests to investigate multi-layer insulation fragments*, in *Space Systems Dynamics Laboratory*. 2008, Kyushu University.
7. Liou, J.-C. and J.K. Weaver. *Orbital Dynamics of High Area-To Ratio Debris and Their Distribution in the Geosynchronous Region*. in

Proceedings of the 4th European Conference on Space Debris. 2005. Darmstadt, Germany.
8. Valk, S., A. Lemaitre, and L. Anselmo, *Analytical and semi-analytical investigations of geosynchronous space debris with high area-to-mass ratio.* Advances in Space Research, 2008. 41.
9. Valk, S. and A. Lemaître, *Semi-analytical investigations of high area-to-mass ratio geosynchronous space debris including Earth's shadowing effects.* Advances in Space Research, 2008. 42.
10. Valk, S., A. Lemaître, and F. Deleflie, *Semi-analytical theory of mean orbital motion for geosynchronous space debris under gravitational influence.* Advances in Space Research, 2008. 43(7): p. 1070-1082.
11. Früh, C. and T. Schildknecht, *Attitude Motion of Space Debris Objects Under Influence of Solar Radiation Pressure And Gravitiy*, in *63rd international Astronautical congress*. 2012: Naples, Italy.
12. Früh, C., T.M. Kelecy, and M.K. Jah, *Coupled Orbit-Attitude Dynamics of High Area-to-Mass Ratio (HAMR) Objects: Influence of Solar Radiation Pressure, Shadow Paths and the Visibility in Light Curves.* Celestial Mechanics and Dynamical Astronomy (CELE), 2013.
13. Früh, C. and M. Jah, *Coupled orbit-attitude motion of high area-to-mass ratio (HAMR) objects including efficient self-shadowing.* Acta Astronautica, 2014. 95: p. 227-241.
14. McMahon, J.W. and D.J. Scheeres. *High-fidelity solar radiation pressure effects for high area-to-mass ratio debris with changing shapes*. in *Proceeding AAS/AIAA Astrodynamics Specialist Conference*. 2013. Hilton Head Island, South Carolina Paper AAS 13-763.
15. Channumsin, S., M. Ceriotti, and G. Radice, *A Deformation model of Flexible, high area-to-mass ratio debris for accurate propagation under perturbation*, in *65th International Astronautical Congress*. 2014: Toronto, Canada.
16. Sheldahl, *The red book*, http://www.sheldahl.com/documents/RedBook%20revised%2020-AUG%20%202012.pdf, Editor. 2012.
17. CAPLINQ, *Technical Data Sheet LINQSTAT PIT1N-ALUM SERIES*. 2012.
18. Rafat, M.Z., M.S. Wheatland, and T.R. Bedding, *Dynamics of a double pendulum with distributed mass.* American Journal of Physics, 2009.
19. Kalman, R.E., *A new approach to linear filtering and prediction problems.* Transaction of the ASME-Journal of Basic Engineering, 1960: p. 35-45.
20. Grewal, S. and P. Andrews, *Kalman Filtering Theory and Practice Using Matlab Grewal*, ed. n. Edition. 2001, New York: John Wiley & Sons Inc.
21. Ryer, D.A., *Light Measurement Handbook*. 1998, United States of America. 64.
22. Vallado, D.A., *Fundamentals of Astrodynamics and Applications*, ed. Third. 2007, New York: Microcosm Press.
23. MICRO-EPSILON, *Instruction Manual optoNCDT 1700*, http://www.micro-epsilon.com/download/manuals/man--optoNCDT-1700--en.pdf, Editor. 2014.